

# Charge localized atomic $\text{Mo}^{\delta+}$ site boosting hydrogen evolution in alkaline solution

**Maoqi Cao**

Central South University

**Kang Liu**

Central South University

**Yao Song**

Central South University of Forestry and Technology

**Chao Ma**

Hunan University <https://orcid.org/0000-0001-8599-9340>

**Yiyang Lin**

Central South University

**Huangjingwei Li**

Central South University

**Junwei Fu**

Central South University

**HongMei Li**

Central South University

**Zhiyan Chen**

Central South University of Forestry and Technology

**Xu-Sheng Zheng**

University of Science and Technology of China

**Junhua Hu**

Zhengzhou University <https://orcid.org/0000-0003-0191-1503>

**Haipeng Xie**

Central South University

**YR Lu**

nsrrc

**Ting-Shan Chan**

National Synchrotron Radiation Research Center <https://orcid.org/0000-0001-5220-1611>

**Min Liu** (✉ [minliu@csu.edu.cn](mailto:minliu@csu.edu.cn))

Central South University <https://orcid.org/0000-0002-9007-4817>

**Keywords:** alkaline HER, single atom alloy (SAA), cobalt (Co), charge localized, N doping

**Posted Date:** November 23rd, 2020

**DOI:** <https://doi.org/10.21203/rs.3.rs-106811/v1>

**License:**   This work is licensed under a Creative Commons Attribution 4.0 International License.

[Read Full License](#)

---

# Abstract

Electrochemical water splitting has drawn tremendous interest for the scalable and sustainable conversion of renewable electricity to clear hydrogen fuel and chemicals. However, the sluggish kinetics of water dissociation step in alkaline solutions restrict severely the application of hydrogen evolution reaction (HER). Here, we designed and prepared cobalt layers with nitrogen modified atomically dispersed Mo sites (N-Mo/Co SAA) to boost the activity of HER. Density functional theory (DFT) calculations demonstrated that the N can induce the asymmetry charge localization of  $\text{Mo}^{\delta+}$  to facilitate the water dissociation. The energy barriers of water dissociation reduced from 0.48 to 0.35 eV by the charge localized  $\text{Mo}^{\delta+}$  site. High resolution transmission electron microscope (HRTEM) and synchrotron X-ray absorption spectroscopy (XAS) measurements confirmed the structure of N modified atomically dispersed  $\text{Mo}^{\delta+}$ . Ambient pressure X-ray photoelectron spectroscopy (AP-XPS) measurements assessed the atomically dispersed  $\text{Mo}^{\delta+}$  site is the active site for water dissociation. Thus, the obtained N-Mo/Co catalyst exhibits record activity with 12 mV overpotential to achieve the current density of  $10 \text{ mA cm}^{-2}$  and Tafel slope of  $31 \text{ mV dec}^{-1}$  in alkaline media, which are superior to 32 mV overpotential for  $10 \text{ mA cm}^{-2}$  and  $38 \text{ mV dec}^{-1}$  Tafel slope on best commercial 20 wt% Pt/C sample in the same condition. This design strategy provided a new pathway to boost the activity of single atom alloy (SAA) by regulating the charge localization of the active site precisely at the atomic-level.

## Introduction

Hydrogen ( $\text{H}_2$ ), as a carbon-free and high density energy source, is of significant importance in the sustainable energy systems and chemical industry.<sup>1-3</sup> Among various  $\text{H}_2$  production methods, electrochemical water splitting in alkaline media has been considered as the most feasible approach for high-purity  $\text{H}_2$  generation in industry.<sup>4,5</sup> However, the sluggish cathodic  $\text{H}_2$  evolution reaction (HER) in alkaline media,<sup>6,7</sup> whose reaction rate is often two or three orders of magnitude lower than that in acidic electrolyte, severely limits the efficiency of water electrolysis.<sup>8,9</sup> Although Pt and Pt-based materials remain the benchmark of HER electrocatalysts,<sup>10-14</sup> their high cost and scarcity greatly hinder their practical applications.<sup>15</sup> Therefore, developing highly efficient and inexpensively alkaline HER catalyst is eagerly.<sup>16-19</sup>

In alkaline solution, hydrogen originate from the water dissociation,<sup>4,20,21</sup> which usually consume tremendously energy and restrict the application of HER.<sup>18,22,23</sup> It has been proved that single atom alloys (SAA) containing atomic water activation component can effectively accelerate the kinetics of alkaline HER.<sup>20,24-26</sup> For example, the Co/Ru single atom alloy (SAA) was reported that the single Co atom reduced the energy barrier of water dissociation and produced hydrogen intermediates that adsorbed on the neighbor Ru sites to generate molecular hydrogen.<sup>20</sup> As a result, the obtained SAA showed a highly improved alkaline HER performance. Similarly, the Ni/Pt SAA exhibited enhanced alkaline HER activity through enhanced OH adsorption on single Ni atom and optimized H adsorption on Pt, respectively.<sup>25</sup>

Although this method has enhanced the activity of Ru and Pt based materials in alkaline media, their activity cannot be continuously adjusted by simply increase the amount of single atoms because the single atom generally show its intrinsic property in noble metal host.<sup>25,27-29</sup> The weak interaction between single atom and noble metal host cannot obviously regulate the electronic state of the single atom site, which restrict the further improvement on performance and practical applications.

In this work, we developed a facile route to controllably modify the electronic structure of Mo single sites to boost the alkaline HER activity through nitrogen doping on non-noble metal Co host. Density functional theory (DFT) calculations shown that the asymmetry charge localization of  $\text{Mo}^{\delta+}$  at N-Mo/Co was induced by doping N. The energy barriers of water dissociation reduced from 0.48 to 0.35 eV at the charge localized  $\text{Mo}^{\delta+}$  site. The HRTEM, SAC-HAADF-STEM, and XAS measurement confirmed the nitrogen modified atomically dispersed Mo in Co layers to form the charge localized  $\text{Mo}^{\delta+}$  site. The AP-XPS was employed to confirm the N lead the asymmetric charge localization of  $\text{Mo}^{\delta+}$  active site in Mo/Co SAA accelerated water dissociation. Compared with bare Mo/Co SAA, the energy barriers of water dissociation reduced from 0.48 to 0.35 eV. Thus, the N-Mo/Co catalyst exhibited a high activity with only 12 mV overpotential to achieve the current density of  $10 \text{ mA cm}^{-2}$  and Tafel slope of  $31 \text{ mV dec}^{-1}$  in alkaline solution. The design strategy greatly boost water dissociation process and decrease the overpotential of HER in alkaline by precisely regulating the charge localization of the active site at the atomic-level.

## Results And Discussion

To investigate the relationship between the electronic structure of active site and water dissociation, we built the Mo/Co and N-Mo/Co SAAs slab model, and calculated the charge density difference, the Bader charge and the energy barrier of water dissociation on catalyst surface (Fig. 1, Supplementary Fig. 1). The charge density difference and Bader charge analyses results show that 0.64 electrons transfer from single atom Mo to substrate in N-Mo/Co, which suggests that an asymmetric charge localization is formed on Mo (Fig. 1a).<sup>9,30,31</sup> The energy barriers of water dissociation on the Co(001), Mo/Co SAA and N-Mo/Co were 0.62, 0.44 and 0.35 eV (Fig. 1b, Supplementary Figs. 1 and 2) respectively, indicating that the asymmetric charge localization of Mo in the N-Mo/Co SAA can improve the water dissociation activity.<sup>32-36</sup>

The water transition state Bader charge analyses performed to prove charge localization  $\text{Mo}^{\delta+}$  can effectively boost water dissociation (Fig. 1c). From the adsorbed water DOS on Mo/Co and N-Mo/Co, we found that the N-Mo/Co leads to the downshift of Mo DOS, which benefit to the activation of water molecule by delocalizing the orbital electron density of the water molecule (Fig. 1d). We also considered the HER activity on Co(101) surface and obtained the same results, proving the charge localization  $\text{Mo}^{\delta+}$  in N-Mo/Co is the key center for water dissociation to promote the kinetics of HER (Supplementary Figs. 3, 4 and 5).

Based on these results, we synthesized Mo/Co SAA and N-Mo/Co by electrochemical reduction precursor in alkaline (Supplementary Figs. 6, 7, 8, 9 and 10). X-ray diffraction (XRD) patterns clearly showed that the Mo/Co and N-Mo/Co are the hexagonal close-packed cobalt structure (Fig. 2a, Supplementary Figs. 11 and 12). From the HRTEM image (Fig. 2b), the interplanar spacing of the main surface is 0.22 nm, which belongs to the Co(001) surface. Spherical aberration corrected high angle annular dark-field scanning TEM (SAC-HAADF-STEM) image (Fig. 2c) showed that the Mo, circled in red, is single-atomic dispersion in N-Mo/Co. In addition, the intensity profiles along X-Y in the HAADF-STEM confirmed the atomically dispersion of Mo in N-Mo/Co (Fig. 2b and 2d). The energy dispersive spectrometer (EDS) mapping images (Fig. 2e) and the line-scan profiles (Supplementary Fig. 13) reveal the Co, Mo and N elements are homogeneously distributed in N-Mo/Co, reveal N has been uniformly doped into the Mo/Co SAA. The electron energy loss spectroscopy (EELS) displays that there is no obvious oxygen in N-Mo/Co (Supplementary Fig. 14). Inductively coupled plasma optical emission spectrometer (ICP-OES) measurement reveals that the concentration of Mo is about 2% doped in N-Mo/Co (Table 1).

To study the electronic structure and local structure of N-Mo/Co, XAS and X-ray photoelectron spectroscopy (XPS) are performed. The K-edges energy of Mo in Mo/Co and N-Mo/Co located between Mo foil and MoO<sub>3</sub> (Fig. 3a), proving the charge localization states of Mo contained in N-Mo/Co. The local structures of Mo in Mo/Co and N-Mo/Co are obtained by extended X-ray absorption fine structure (EXAFS) spectrometer. In the Fig. 3b, Mo/Co SAA shows a coordination peak at 2.18 Å corresponding to the crystal structure of Co. After the N doped into the Mo/Co SAA, a new peak located at 1.56 Å arises, indicating the N-Mo bond formed.<sup>37</sup>

Figure 3c shows the Co L-edge spectra of Co, Mo/Co and N-Mo/Co, the two peaks located at 778 eV and 795 eV corresponds to the electron transition from Co 2P<sub>3/2</sub> and 2P<sub>1/2</sub> to 3d, respectively. Compared with Co, the binding energy of Co in N-Mo/Co displays a positive shift of about 0.2 eV to higher energy region due to the N doping.<sup>38</sup> Meanwhile, similar shift of Co was also found in the Co K-edge of N-Mo/Co (Supplementary Fig. 15). For the sample of N-Mo/Co, the peaks at 398.3 and 399.9 eV can be attribute to Mo 3p<sub>3/2</sub> and N (Fig. 3d),<sup>26</sup> respectively, confirming that the nitrogen was doped in the Mo/Co SAA surface to form the N-Mo/Co (Supplementary Fig. 16).

The ultraviolet photoelectron spectrometer (UPS) (Supplementary Fig. 17) indicates that the d band center of N-Mo/Co shifts away from the Fermi level after N doped in Mo/Co, suggesting that the interaction of Mo and N makes a significant contribution to valence band structure of N-Mo/Co, which is consistent with DOS analysis (Fig. 1d). Overall, all these results demonstrate that the atomically dispersed charge localization site of Mo<sup>δ+</sup> has been built in N-Mo/Co SAA.

The AP-XPS was performed to confirm the active sites of water dissociation on N-Mo/Co.<sup>2</sup> Fig. 4a and 4b show the curve-fitting of the O 1s XPS spectra for N-Mo/Co under ultrahigh vacuum (UHV) and water pressure of 0.15 torr. The obvious OH and chemisorbed H<sub>2</sub>O on the surface are observed under water pressure of 0.15 torr, suggesting efficient water dissociation on the sample of N-Mo/Co. Figure 4c and 4d

shows the Co 2p and Mo 3d XPS spectra of N-Mo/Co under UHV and 0.15 torr water pressure. The binding energies of Co 2p<sub>3/2</sub> and Co 2p<sub>1/2</sub> have little change in water condition. However, the binding energies of Mo 3d<sub>5/2</sub> and Mo 3d<sub>3/2</sub> shows an obvious positive shift of about 0.3 eV in water condition. These results further confirm that atomically dispersed asymmetry charge localization site of Mo<sup>δ+</sup> is the active site of water dissociation.

To verify the catalytic activity of Mo sites in N-Mo/Co, the electrocatalytic performance for HER is evaluated by using a three-electrode system in 1.0 M KOH solution, with Hg/HgO as the reference electrode and graphite rod as the counter electrode, respectively. The linear sweep voltammetry (LSV) curves of Co, Mo/Co, N-Mo/Co and commercial Pt/C clearly shows that N-Mo/Co exhibits the best performance among all samples (Fig. 5a). The overpotential to achieve the current density of 10 mA cm<sup>-2</sup> is only 12 mV, significantly better than those of Co (209 mV), Mo/Co (82 mV) and even the commercial 20 wt% Pt/C (32 mV). In Fig. 5b, the derived Tafel slopes of Co and Mo/Co are 129 and 89 mV dec<sup>-1</sup>, indicating that the water dissociation is the rate-determining step on Co and Mo/Co. However, the Tafel slope of N-Mo/Co decreases to 31 mV dec<sup>-1</sup>, which is even better than Pt/C (38 mV dec<sup>-1</sup>), suggesting that the atomically dispersed charge localization of Mo<sup>δ+</sup> site can improve the intrinsic water dissociation activity of N-Mo/Co for alkaline HER. The N-Mo/Co catalyst exhibits record activity in alkaline media (Fig. 5c). The turnover frequency (TOF) values of N-Mo/Co is also obviously larger than Mo/Co (Fig. 5d, Supplementary Fig. 18), revealing the superior intrinsic HER activity of N-Mo/Co. The electrochemical impedance spectroscopy (EIS) results shows that the charge-transfer resistance (R<sub>ct</sub>) of N-Mo/Co is only 1.7 Ω, much lower than those of Co (95.6 Ω) and Mo/Co (6.5 Ω), suggesting that the N doped in Mo/Co SAA can promote charge transport kinetics (Supplementary Fig. 19).

To assess the energy barriers of HER, we studied the effect of temperature on the performance of the catalysts and found the rate constants to follow the Arrhenius relationship. The Arrhenius plots for the Co, Mo/Co and N-Mo/Co catalysts allowed us to extract electrochemical activation energies for hydrogen production (Fig. 5e, Supplementary Fig. 20). It shows that N-Mo/Co exhibits an apparent barrier value of 10.8 kJ mol<sup>-1</sup>, which is significantly lower than those of Co (30.0 kJ mol<sup>-1</sup>) and Mo/Co SAA (18.2 kJ mol<sup>-1</sup>) catalyst, indicating the obviously accelerated kinetic process of HER on N-Mo/Co catalyst. Furthermore, the durability test of N-Mo/Co electrode at potential of 12 mV was performed to evaluate the stability of the N-Mo/Co (Fig. 5f). The catalyst exhibits an initial current density of 10 mA cm<sup>-2</sup>, and there is no obvious decrease after 200 h test, indicating its excellent electrochemical stability for long-term operation. The Faradaic efficiency remained about 100% in the HER process.

Inspired by such excellent HER activity, we also assemble a water-alkali electrolyzer with N-Mo/Co as cathode and anode simultaneously to evaluate its potential for overall water splitting. The cell voltage needed only 1.5 V to give a current density of 10 mA cm<sup>-2</sup> and it presented a negligible loss after a long time test of about 45 h (Supplementary Fig. 21). These results fully demonstrated that the N-induced atomically dispersed charge localization site of Mo<sup>δ+</sup> on N-Mo/Co has high water dissociation activity and stability.

# Conclusion

In summary, we have designed and prepared the atomically dispersed charge localization of  $\text{Mo}^{\delta+}$  in N-Mo/Co. DFT calculations and fine-structural characterization present that the N doped in Mo/Co SAA leading to the asymmetry charge localization of  $\text{Mo}^{\delta+}$  site in N-Mo/Co. The ambient pressure XPS (AP-XPS) further demonstrate the charge localization of Mo site can facilitate water dissociation. The obtained N-Mo/Co catalyst exhibits a high activity with only 12 mV overpotential to achieve the current density of  $10 \text{ mA cm}^{-2}$  and Tafel slope of  $31 \text{ mV dec}^{-1}$ , showing a big progress in the field. This work provides a new design insight at atomic scale for SAA catalysts to boost the activity of HER in alkaline media.

# Methods

**Materials synthesis.** Generally, the N-Mo/Co single atom alloy (SAA) was obtained through a three-step process. First,  $\text{CoMoO}_4$  on carbon cloth (CC) was synthesized via a modified hydrothermal method. Then, N- $\text{CoMoO}_4$  was prepared by nitridation of the  $\text{CoMoO}_4$  at  $330 \text{ }^\circ\text{C}$  in a home-built tube furnace using ammonia gas as nitridation source. Finally, N-Mo/Co was obtained by in-situ electrochemical reduction at constant voltage of  $-0.5 \text{ V}$  (RHE).

All of the chemical reagents were analytical grade (AR) and purchased from Aladdin. They were all used directly without any further purification. The deionized water (DI) used in all experiments was produced from water purification apparatus of Milli-Q ( $18.2 \text{ M}\Omega \text{ cm}^{-1}$ ).

The precursor of  $\text{CoMoO}_4$  supported on CC was synthesized via a modified method. First, a piece of CC substrates ( $2 \times 4 \text{ cm}$ ) were pretreated in concentrated nitric acid at  $80 \text{ }^\circ\text{C}$  for 2 h to remove the surface impurity and improve the surface hydrophilicity. Then, 10 mmol  $\text{Co}(\text{NO}_3)_2 \cdot 6\text{H}_2\text{O}$ , 1.5 mmol  $(\text{NH}_4)_6\text{Mo}_7\text{O}_{24}$ , 50 mmol  $\text{CO}(\text{NH}_2)_2$  and 20 mmol  $\text{NH}_4\text{F}$  were dissolved in 200 ml DI water under vigorously stirring to form a transparent wine red solution. The 40 mL prepared solution and a piece of treated carbon cloth were then transferred into a 50 mL Teflon-lined autoclave, which was sealed and heated in oven at  $120 \text{ }^\circ\text{C}$  for 4 h. After naturally cooling down to room temperature, the precursor of  $\text{CoMoO}_4$  on CC were taken out from the autoclaves and further washed with water and ethanol for three times, followed by drying at  $60 \text{ }^\circ\text{C}$  for 12 h in oven. The precursor of Co on CC was prepared as  $\text{CoMoO}_4$  without  $(\text{NH}_4)_6\text{Mo}_7\text{O}_{24}$ .

The  $\text{CoMoO}_4$  was obtained by heat treatment of the precursor at  $330 \text{ }^\circ\text{C}$  in a home-built tube furnace using Ar gas as the carrier gas and the N- $\text{CoMoO}_4$  was prepared by the same method using ammonia gas as carrier gas and nitridation source. The prepared  $\text{CoMoO}_4$  is transformed into Mo dopant cobalt oxyhydroxide (Mo-CoOOH) after in 1 M KOH solution for 2 hours, which is supported by XRD and ICP-OES analysis of the samples before and after phase transition. Inspired by the novel phenomenon of  $\text{CoMoO}_4$  in alkaline solution, The Mo/Co and N-Mo/Co can be probably prepared by electrochemical reduction of  $\text{CoMoO}_4$  and N- $\text{CoMoO}_4$  in alkaline solution. The cathodic currents of  $\text{CoMoO}_4$  and N- $\text{CoMoO}_4$  at

constant voltage of  $-0.5$  V (RHE) gradually becomes larger at the initial time of about 2 hours, suggesting the possible significant structure changes in the electrochemical process. XRD patterns SEM clearly indicate the  $\text{CoMoO}_4$  and  $\text{N-CoMoO}_4$  become hexagon flake structure of Co after electrochemical reduction in alkaline for 4 hours. The sample of Co on CC is prepared by electrochemical reduction of the  $\text{Co}(\text{CO}_3)_x\text{OH}_y$  precursor with the same method. The synthesis of precursor of Co on CC was prepared as the N-Mo/Co without adding  $(\text{NH}_4)_6\text{Mo}_7\text{O}_{24}$ .

**Characterization.** The X-ray diffraction (XRD) patterns were obtained on a Bruker D8 Discover X-ray diffractometer using monochromatized  $\text{Cu K}\alpha$  ( $\lambda = 1.5406 \text{ \AA}$ ) as radiation source with a scanning step of  $0.02^\circ$  per second from  $5^\circ$  to  $80^\circ$ . The morphology and structure of the obtained samples were characterized by field-emission SEM (NOVA NANOSEM 450), TEM, HAADF-STEM and EELS (Talos F200X and JEMARM 200F). The XPS measurements were performed on an ESCALAB250Xi spectrometer (Thermo Scientific) using  $\text{Al K}\alpha$  ( $1486.68 \text{ eV}$ ) as X-ray source.

**XAFS and AP-XPS measurements and analysis.** The EXAFS and XANES of Co K-edge and Mo K-edge were performed at BL01C1 station of National Synchrotron Radiation Research Center, Taiwan. The transmission and fluorescence modes were used for collecting data of Co and Mo K-edge respectively at room temperature. The raw data of EXAFS were processed following the standard procedures with the software packages of ATHENA. The final EXAFS spectra were obtained after removing the post-edge background and normalizing the edge-jump step. The soft XANES of Co L-edge and N K-edge were carried out at beamline BL10B of National Synchrotron Radiation Laboratory (NSRL) in Hefei, China. The total electron yield mode was used for collecting the data of Co L-edge under an ultrahigh vacuum of  $5 \times 10^{-10}$  mbar. The photon flux was about  $10^{10}$  and the energy resolution is about 1000 (E/ $\Delta$ E). The energy range between 760 and 805 eV was used to obtain the Co L-edge absorption spectrum. The soft XANES original data were processed using a common strategy with several steps. The energy of absorption spectrum was calibrated firstly with the Au 4f peak as a standard and then the pre-edge of substrate was set zero. At last, the edge-jump of the obtained spectra was normalized to one. The ultraviolet photoemission spectroscopy spectra were performed at BL10B of NSRL with the excitation energy of 170 eV.

Ambient-pressure XPS (AP-XPS) studies were performed at the National Synchrotron Radiation Research Center in Taiwan, at beam-line 24A1. The calibration of the binding energy (BE) scale was carried out using the Au 4f photoelectron peak as reference ( $4f_{7/2}$  BE = 84.0 eV), from a clean gold polycrystalline surface. The XPS peak shapes were fitted with XPS Peak software using a Shirley background.

**Electrochemical measurements.** All electrochemical measurements were performed on an electrochemical workstation of Princeton 4000A using a three-electrode system with the as-prepared samples as working electrode, the graphite rod and Hg/HgO as the counter and reference electrode respectively. The sample of Pt/C was obtained by dropping the uniform ink of Pt/C (20%) on carbon cloth ( $1.0 \text{ mg cm}^{-2}$ ) where the Pt/C ink was prepared by ultrasonic dispersion of 10 mg Pt/C (20%) and 150  $\mu\text{L}$  5 wt% Nafion solution in 2.5 ml water/isopropanol (v/v 4:1) solution. All potentials used in this work were converted to the values versus reversible hydrogen electrode (RHE) with the equation  $E_{\text{RHE}} = E_{\text{SCE}} + 0.0591$

$\times \text{pH} + 0.241 \text{ V}$ . The scan rate of 2 mV/s was used in the measurements of LSV. The overpotential of 50 mV with perturbation amplitude of 10 mV was performed in the measurements of electrochemical impedance spectroscopy (EIS) in the frequency from 100 kHz to 0.001 Hz. The cyclic voltammograms (CVs) in the range between 0.01 and 0.11 V was used to estimate the electrochemical surface areas (ECSA) at the scan rates of 20, 40, 60, 80 and 100  $\text{mV s}^{-1}$ , respectively. The difference values of current density per square centimeter ( $\text{cm}^2$ ) at 0.06 V vs RHE were plotted with the scan rates in which the slope was used to measure the ECSA. The quantification of the produced hydrogen was performed with a thermal conductivity detector (TCD) of gas chromatography (GC 2014 C SHIMADZU).

For temperature-dependent measurements, the electrochemical reaction cell with electrodes was put in a water bath. The temperature was first improved to the value above 60 °C, then the current values of catalyst at temperature of 60, 55, 50, 45, 40, 35, 30 and 25 °C were recorded with the temperature reducing in environment in order to decrease error. The performance of different catalysts at various temperatures is shown in table 1. As we all know, the kinetics of chemical reactions increases with the temperature rising which is the same with HER. The relation of chemical rate constant with the temperature is about proportional to  $\exp(-\Delta H^*/kT)$ , where  $\Delta H^*$  and  $k$  is the activation energy and the Boltzmann constant respectively. Specially, the approximate activation energy ( $E_a$ ) for HER can be defined by the Arrhenius relationship

$$\ln i_k = -\frac{E_a}{RT} + C$$

Where  $T$  is the test temperature,  $i_k$  is the current at  $\eta = -200 \text{ mV}$  and  $R$  is the gas equilibrium constant. The linear dependence on temperature of Arrhenius plots for four various catalysts are displayed in Fig. 3d. The  $E_a$  for different HER catalysts can be obtained by the slopes of various Arrhenius plots ( $-R \times \text{slope}$ ).

**Details of DFT calculations.** Our density functional theory (DFT) simulations were performed using the Vienna ab initio simulation package (VASP).<sup>39-41</sup> Core - valence interactions was described by the projector augmented wave (PAW) method.<sup>42</sup> The Perdew-Burke-Ernzerh (PBE) functional within the generalized gradient approximation was used to describe the exchange and correlation functional.<sup>43</sup> The cutoff energy of 400 eV was set in our calculations, and  $2 \times 2 \times 1$  Monkhorst-Pack  $k$  grids are applied during the optimization. We built four layer Co(001) and Co(101) slab with vacuum layer 15 Å. During the geometry optimizations, the bottom two-layers were fixed while the remaining layers were allowed to relax. Transition states (TS) were located by a combination of the Nudged Elastic Band (CI-NEB) and the Improved Dimer Method (IDM).<sup>44-46</sup> All TS structures have a single imaginary frequency. The iterative process considered was convergences, when the force on the atom was less than  $0.02 \text{ eV \AA}^{-1}$  and the energy change was less than  $10^{-5} \text{ eV}$  per atom. We used the VESTA package to visualize the structures and charge density differences.<sup>47</sup>

The Gibbs free energy of H\* step was calculated as

$$\Delta G = \Delta E + \Delta ZPE - T \cdot \Delta S$$

Where  $\Delta E$  is reaction energy calculated from DFT.  $\Delta ZPE$  and  $\Delta S$  are the changes in zero-point energy and entropy during the reaction, respectively.<sup>48–50</sup>

### Data availability

The data that support the findings of this study are available from the corresponding author on reasonable request.

## Declarations

## Conflicts of interest

There are no conflicts to declare.

## Contributions

M. Liu and H. Li conceived the project; M. Cao, K. Liu, Y. Song and M. Liu designed the experiments and analyzed the results. M. Cao and Y. Lin synthesized the samples, performed the electrochemical experiments and analysed the results. K. Liu and H. Li carried out the simulations and wrote the corresponding section. K. Liu, Y. Lin, X. Zheng, Y. Lu, and T. C. conducted the XAS measurements. K. Liu, Y. Lin and H. Xie conducted the XPS measurements. H.J.W. Li, J. Fu, Z. Chen and J. H. carried out the electron microscope measurements. All authors read and commented on the manuscript.

## Acknowledgements

The authors gratefully thank the International Science and Technology Cooperation Program (Grant No. 2017YFE0127800 and 2018YFE0203400), Natural Science Foundation of China (Grant No. 21872174 and U1932148), Hunan Provincial Science and Technology Program (No.2017XK2026), Shenzhen Science and Technology Innovation Project (Grant No. JCYJ20180307151313532). This work benefited from Taiwan Beam Lines BL01C1, and BL24A1 in the National Synchrotron Radiation Research Center, (Grant No. MOST 109-2113-M-213-002).

## References

1. Turner, J. A. Sustainable hydrogen production. *Science* **305**, 972–974 (2004).

- Dinh, C.-T. *et al.* Multi-site electrocatalysts for hydrogen evolution in neutral media by destabilization of water molecules. *Nat. Energy* **4**, 107–114 (2018).
- Jiao, Y., Zheng, Y., Jaroniec, M. & Qiao, S. Z. Design of electrocatalysts for oxygen- and hydrogen-involving energy conversion reactions. *Chem. Soc. Rev.* **44**, 2060–2086 (2015).
- Wang, X., Zheng, Y., Sheng, W., Xu, Z. J., Jaroniec, M. & Qiao, S.-Z. Strategies for design of electrocatalysts for hydrogen evolution under alkaline conditions. *Mater. Today* **36**, 125–138 (2020).
- Mahmood, N., Yao, Y., Zhang, J. W., Pan, L., Zhang, X. & Zou, J. J. Electrocatalysts for hydrogen evolution in alkaline electrolytes: mechanisms, challenges, and prospective solutions. *Adv. Sci.* **5**, 1700464 (2018).
- Luo, Y. *et al.* Two-dimensional MoS<sub>2</sub> confined Co(OH)<sub>2</sub> electrocatalysts for hydrogen evolution in alkaline electrolytes. *ACS Nano* **12**, 4565–4573 (2018).
- Subbaraman, R. *et al.* Enhancing hydrogen evolution activity in water splitting by tailoring Li<sup>+</sup>-Ni(OH)<sub>2</sub>-Pt interfaces. *Science* **334**, 1256–1260 (2011).
- Yin, J. *et al.* Atomic arrangement in metal-doped NiS<sub>2</sub> boosts the hydrogen evolution reaction in alkaline media. *Angew. Chem. Int. Ed.* **58**, 18676–18682 (2019).
- Liu, D. *et al.* Atomically dispersed platinum supported on curved carbon supports for efficient electrocatalytic hydrogen evolution. *Nat. Energy* **4**, 512–518 (2019).
- Zhang, J. *et al.* Single platinum atoms immobilized on an MXene as an efficient catalyst for the hydrogen evolution reaction. *Nat. Catal.* **1**, 985–992 (2018).
- Zhang, L. *et al.* Atomic layer deposited Pt-Ru dual-metal dimers and identifying their active sites for hydrogen evolution reaction. *Nat. Commun.* **10**, 4936 (2019).
- Lao, M. *et al.* Platinum/nickel bicarbonate heterostructures towards accelerated hydrogen evolution under alkaline conditions. *Angew. Chem. Int. Ed.* **58**, 5432–5437 (2019).
- Kim, J. *et al.* Theoretical and experimental understanding of hydrogen evolution reaction kinetics in alkaline electrolytes with Pt-based core-shell nanocrystals. *J. Am. Chem. Soc.* **141**, 18256–18263 (2019).
- Zhao, Z. *et al.* Surface-engineered PtNi-O nanostructure with record-high performance for electrocatalytic hydrogen evolution reaction. *J. Am. Chem. Soc.* **140**, 9046–9050 (2018).
- Ling, T. *et al.* Well-dispersed nickel- and zinc-tailored electronic structure of a transition metal oxide for highly active alkaline hydrogen evolution reaction. *Adv. Mater.* **31**, e1807771 (2019).
- Roger, I., Shipman, M. A. & Symes, M. D. Earth-abundant catalysts for electrochemical and photoelectrochemical water splitting. *Nat. Rev. Chem.* **1**, 0003 (2017).
- Zhu, Y. P., Guo, C., Zheng, Y. & Qiao, S.-Z. Surface and interface engineering of noble-metal-free electrocatalysts for efficient energy conversion processes. *Acc. Chem. Res.* **50**, 915–923 (2017).
- Lei, C. *et al.* Efficient alkaline hydrogen evolution on atomically dispersed Ni–Nx Species anchored porous carbon with embedded Ni nanoparticles by accelerating water dissociation kinetics. *Energy Environ. Sci.* **12**, 149–156 (2019).

19. Wang, H. *et al.* Bifunctional non-noble metal oxide nanoparticle electrocatalysts through lithium-induced conversion for overall water splitting. *Nat. Commun.* **6**, 7261 (2015).
20. Mao, J. *et al.* Accelerating water dissociation kinetics by isolating cobalt atoms into ruthenium lattice. *Nat. Commun.* **9**, 4958 (2018).
21. Zhang, J. *et al.* Engineering water dissociation sites in MoS<sub>2</sub> nanosheets for accelerated electrocatalytic hydrogen production. *Energy Environ. Sci.* **9**, 2789–2793 (2016).
22. Xu, K. *et al.* Regulating water-reduction kinetics in cobalt phosphide for enhancing HER catalytic activity in alkaline solution. *Adv. Mater.* **29**, 1606980 (2017).
23. Zheng, Y., Jiao, Y., Qiao, S. & Vasileff, A. The hydrogen evolution reaction in alkaline solution: From theory, single crystal models, to practical electrocatalysts. *Angew. Chem. Int. Ed.* **57**, 7568–7579 (2018).
24. Chao, T. *et al.* Atomically dispersed copper-platinum dual sites alloyed with palladium nanorings catalyze the hydrogen evolution reaction. *Angew. Chem. Int. Ed.* **56**, 16047–16051 (2017).
25. Li, M. *et al.* Single-atom tailoring of platinum nanocatalysts for high-performance multifunctional electrocatalysis. *Nat. Catal.* **2**, 495–503 (2019).
26. Cao, B., Veith, G. M., Neuefeind, J. C., Adzic, R. R. & Khalifah, P. G. Mixed close-packed cobalt molybdenum nitrides as non-noble metal electrocatalysts for the hydrogen evolution reaction. *J. Am. Chem. Soc.* **135**, 19186–19192 (2013).
27. Greiner, M. T. *et al.* Free-atom-like d states in single-atom alloy catalysts. *Nat. Chem.* **10**, 1008–1015 (2018).
28. Qin, X. *et al.* The role of Ru in improving the activity of Pd toward hydrogen evolution and oxidation reactions in alkaline solutions. *ACS Catal.* **9**, 9614–9621 (2019).
29. Yao, Y. *et al.* Engineering the electronic structure of single atom Ru sites via compressive strain boosts acidic water oxidation electrocatalysis. *Nat. Catal.* **2**, 304–313 (2019).
30. Wei, Y. *et al.* New strategy for designing orangish-redemitting phosphor via oxygen-vacancy-induced electronic localization. *Light Sci. Appl.* **8**, 15 (2019).
31. Zhou, Y. *et al.* Dopant-induced electron localization drives CO<sub>2</sub> reduction to C<sub>2</sub> hydrocarbons. *Nat. Chem.* **10**, 974–980 (2018).
32. Zhang, L. *et al.* Charge polarization from atomic metals on adjacent graphitic layers for enhancing the hydrogen evolution reaction. *Angew. Chem. Int. Ed.* **58**, 9404–9408 (2019).
33. Chen, K. *et al.* Iron phthalocyanine with coordination induced electronic localization to boost oxygen reduction reaction. *Nat. Commun.* **11**, 4173 (2020).
34. Fu, J. *et al.* Graphitic carbon nitride with dopant induced charge localization for enhanced photoreduction of CO<sub>2</sub> to CH<sub>4</sub>. *Adv. Sci.* **6**, 1900796 (2019).
35. Liu, K. *et al.* Single-atom transition metals supported on black phosphorene for electrochemical nitrogen reduction. *Nanoscale* **12**, 4903–4908 (2020).

36. You, B. *et al.* Universal surface engineering of transition metals for superior electrocatalytic hydrogen evolution in neutral water. *J. Am. Chem. Soc.* **139**, 12283–12290 (2017).
37. Han, L. *et al.* Atomically dispersed molybdenum catalysts for efficient ambient nitrogen fixation. *Angew. Chem. Int. Ed.* **58**, 2321–2325 (2019).
38. Wu, Y. *et al.* Electron density modulation of NiCo<sub>2</sub>S<sub>4</sub> nanowires by nitrogen incorporation for highly efficient hydrogen evolution catalysis. *Nat. Commun.* **9**, 1425 (2018).
39. Kresse, G. & Furthmüller, J. Efficiency of ab-initio total energy calculations for metals and semiconductors using a plane-wave basis set. *Comput. Mater. Sci.* **6**, 15–50 (1996).
40. Kresse, G. & Furthmüller, J. Efficient iterative schemes for ab initio total-energy calculations using a plane-wave basis set. *Phys. Rev. B* **54**, 11169–11856 (1996).
41. Kresse, G. & Hafner, J. Ab initio molecular-dynamics simulation of the liquid-metal-amorphous-semiconductor transition in germanium. *Phys. Rev. B* **49**, 14251–14269 (1994).
42. Blochl, P. E. Projector augmented-wave method. *Phys. Rev. B* **50**, 17953–17979 (1994).
43. Perdew, J. P., Burke, K. & Ernzerhof, M. Generalized gradient approximation made simple. *Phys. Rev. Lett.* **78**, 1396 (1996).
44. Henkelman, G. & Jónsson, H. Improved tangent estimate in the nudged elastic band method for finding minimum energy paths and saddle points. *J. Chem. Phys.* **113**, 9978 (2000).
45. Henkelman, G., Uberuaga, B. P. & Jónsson, H. A climbing image nudged elastic band method for finding saddle points and minimum energy paths. *J. Chem. Phys.* **113**, 9901–9904 (2000).
46. Heyden, A., Bell, A. T. & Keil, F. J. Efficient methods for finding transition states in chemical reactions: comparison of improved dimer method and partitioned rational function optimization method. *J. Chem. Phys.* **123**, 224101 (2005).
47. Momma, K. & Izumi, F. VESTA3 for three-dimensional visualization of crystal, volumetric and morphology data. *J. Appl. Crystallogr.* **44**, 1272–1276 (2011).
48. Peterson, A. A., Abild-Pedersen, F., Studt, F., Rossmeisl, J. & Nørskov, J. K. How copper catalyzes the electroreduction of carbon dioxide into hydrocarbon fuels. *Energy Environ. Sci.* **3**, 1311–1315 (2010).
49. Nørskov, J. K. *et al.* Origin of the overpotential for oxygen reduction at a fuel-cell cathode. *J. Phys. Chem. B* **108**, 17886–17892 (2004).
50. Nørskov, J. K. *et al.* Trends in the exchange current for hydrogen evolution. *J. Electrochem. Soc.* **152**, J23 (2005).

## Figures

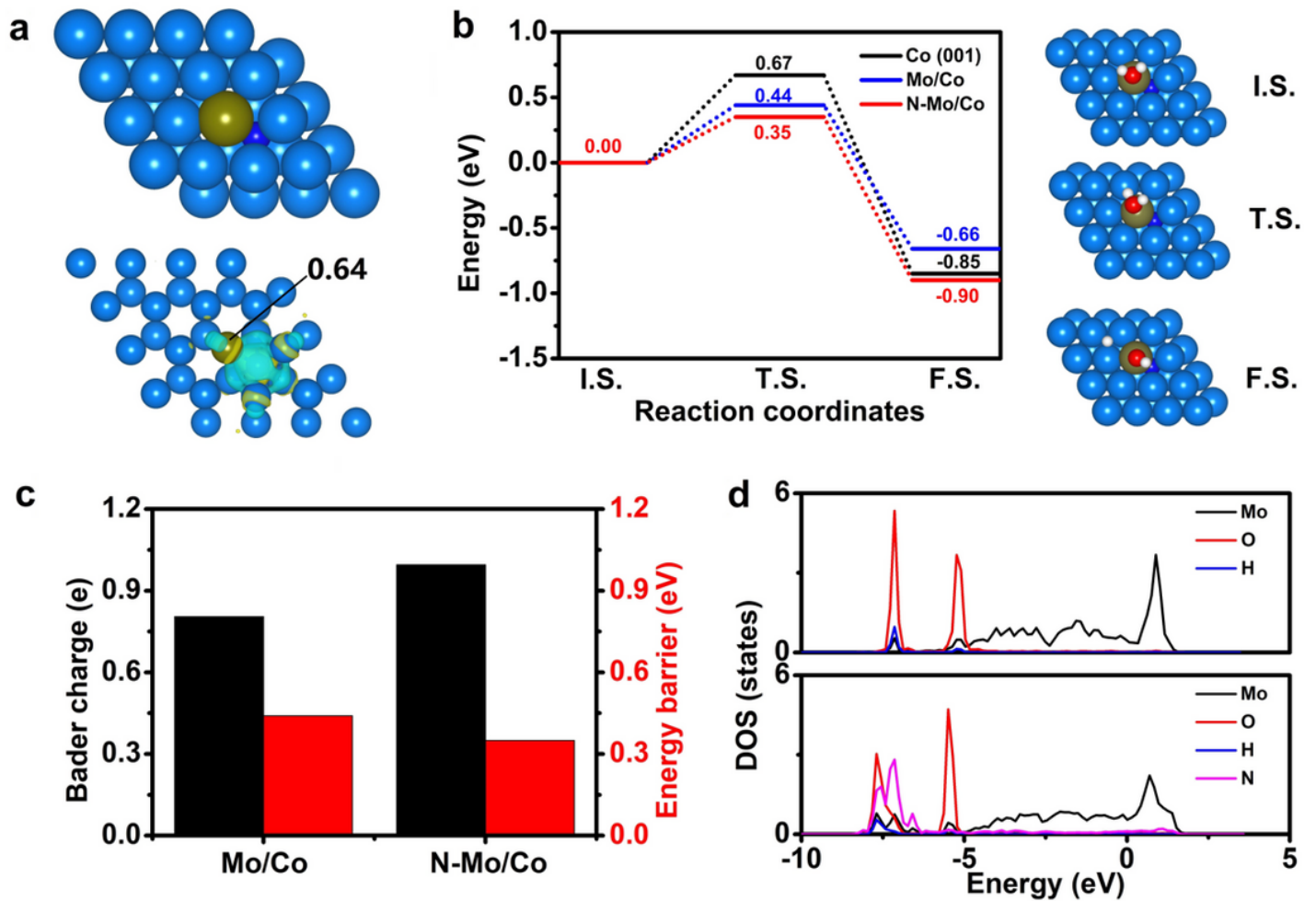


Figure 1

The design and DFT calculations of catalyst. (a) The configuration and the charge localization difference of Mo site on Mo/Co and N-Mo/Co. (b) The energy barrier of water dissociation on the Co, Mo/Co and N-Mo/Co. Initial state denote as I.S.. Transition state denote as T.S.. Final state denote as F.S.. (c) The relationship between Bader charge and energy barrier at the transition state. (d) The density of state of water adsorb on the Mo/Co and N-Mo/Co.

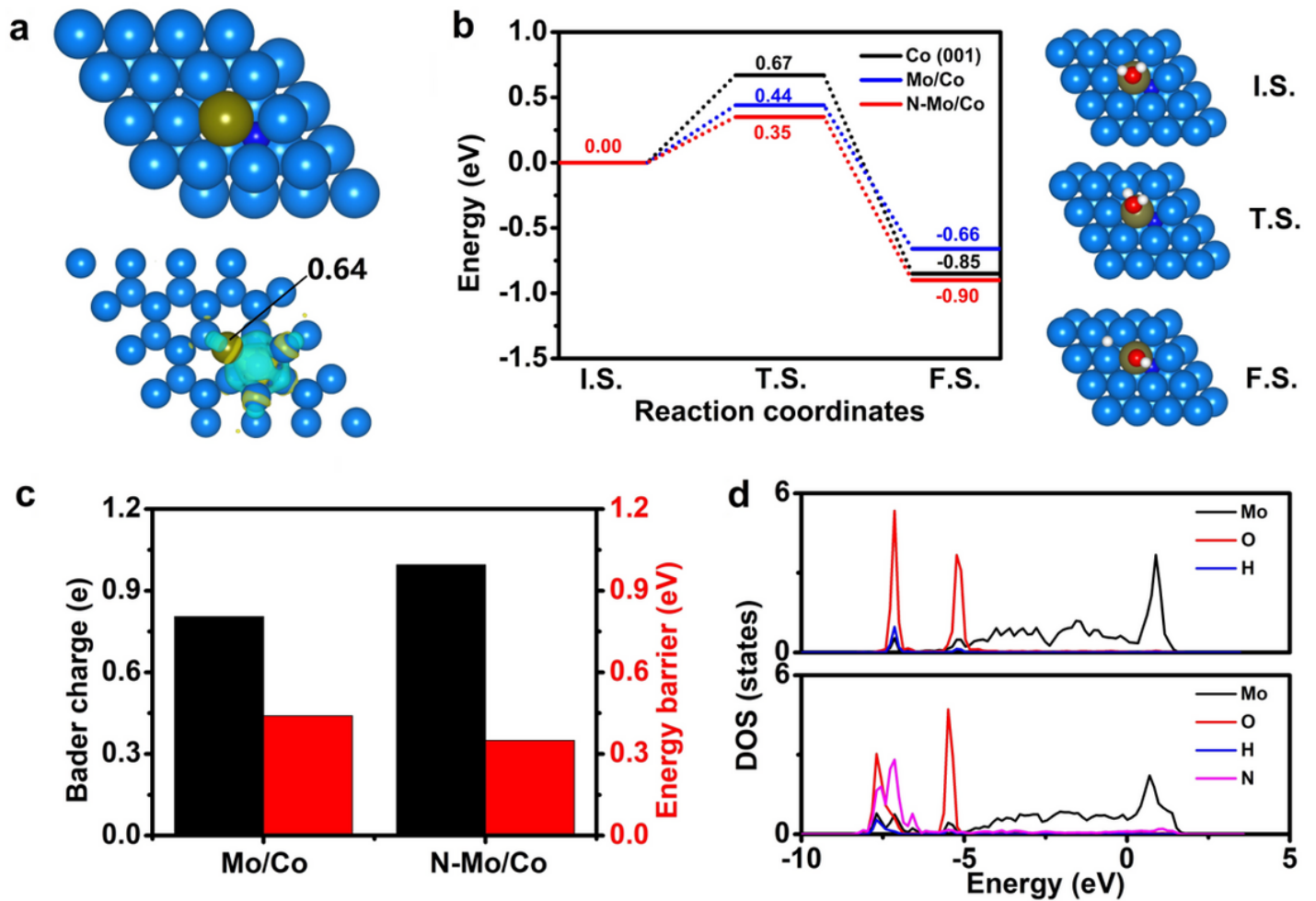
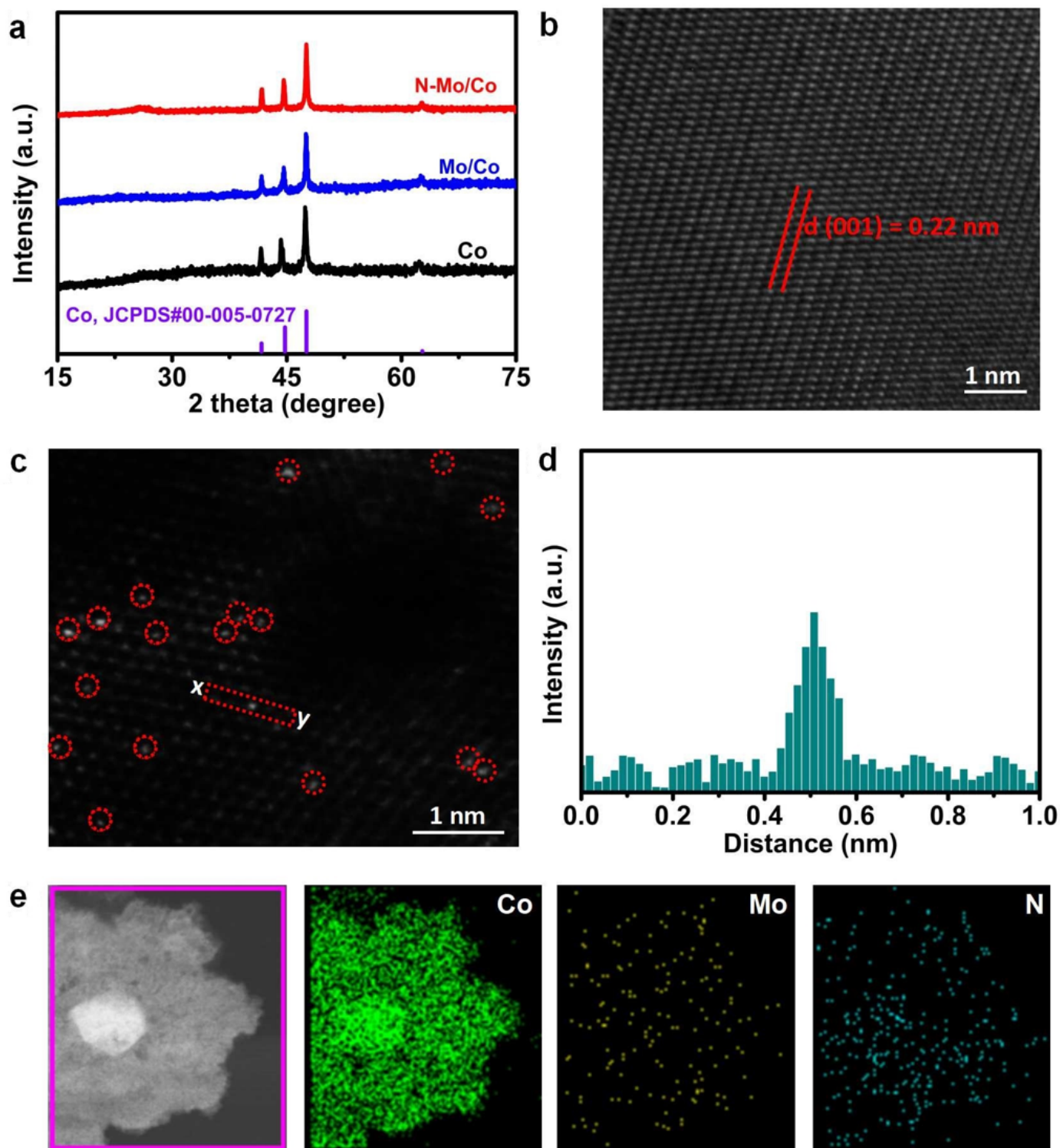


Figure 1

The design and DFT calculations of catalyst. (a) The configuration and the charge localization difference of Mo site on Mo/Co and N-Mo/Co. (b) The energy barrier of water dissociation on the Co, Mo/Co and N-Mo/Co. Initial state denote as I.S.. Transition state denote as T.S.. Final state denote as F.S.. (c) The relationship between Bader charge and energy barrier at the transition state. (d) The density of state of water adsorb on the Mo/Co and N-Mo/Co.



**Figure 2**

Characterization of N-Mo/Co. (a) XRD patterns of Co, Mo/Co and N-Mo/Co. (b) HR-TEM image of N-Mo/Co. The scale bar is 1 nm. (c) SAC-HAADF-STEM image of N-Mo/Co. The scale bar is 1 nm. (d) Intensity profiles along X-Y in the SAC-HAADF-STEM image. (e) Element mapping images of Co, Mo and N in N-Mo/Co.

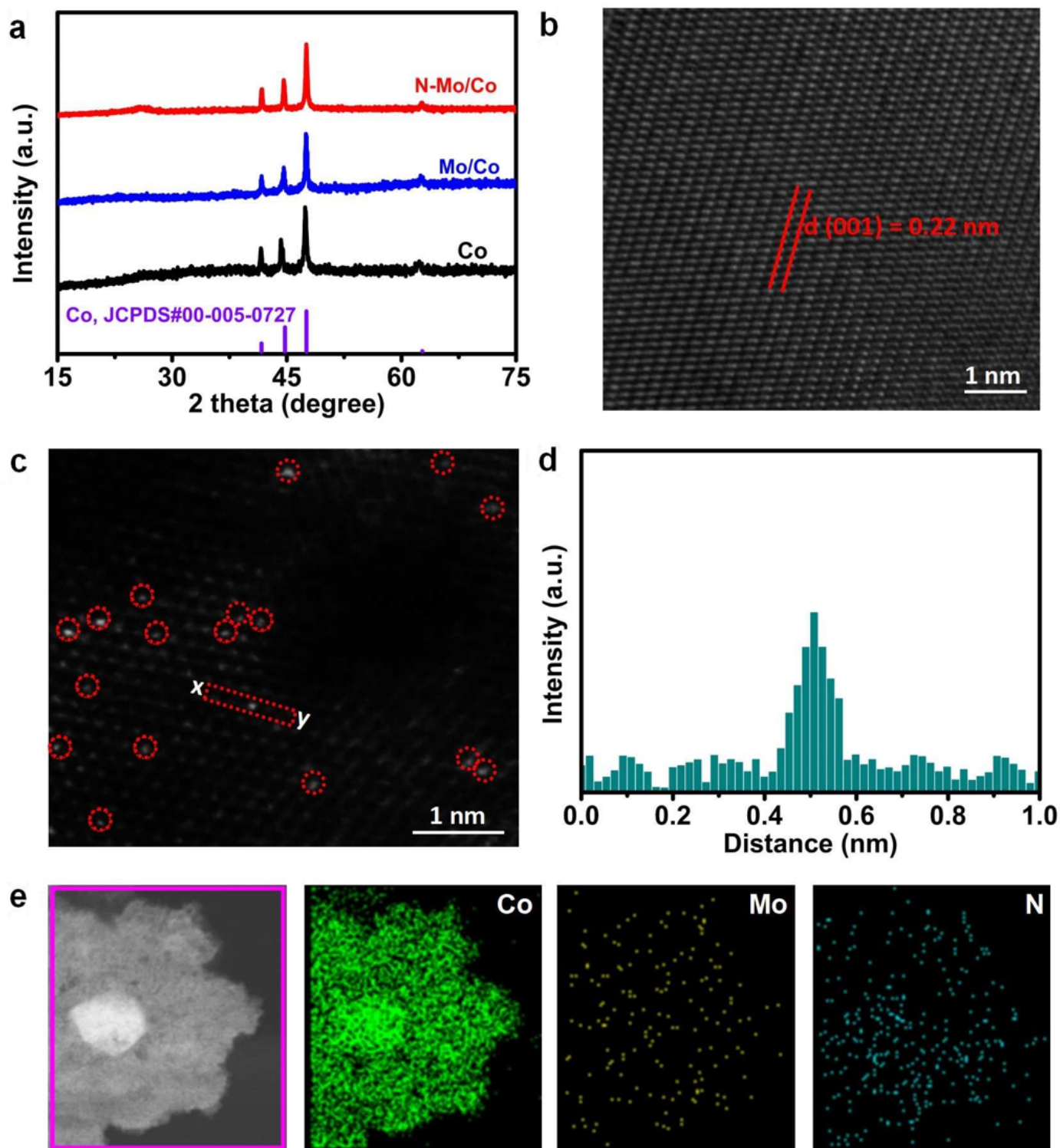


Figure 2

Characterization of N-Mo/Co. (a) XRD patterns of Co, Mo/Co and N-Mo/Co. (b) HR-TEM image of N-Mo/Co. The scale bar is 1 nm. (c) SAC-HAADF-STEM image of N-Mo/Co. The scale bar is 1 nm. (d) Intensity profiles along X-Y in the SAC-HAADF-STEM image. (e) Element mapping images of Co, Mo and N in N-Mo/Co.

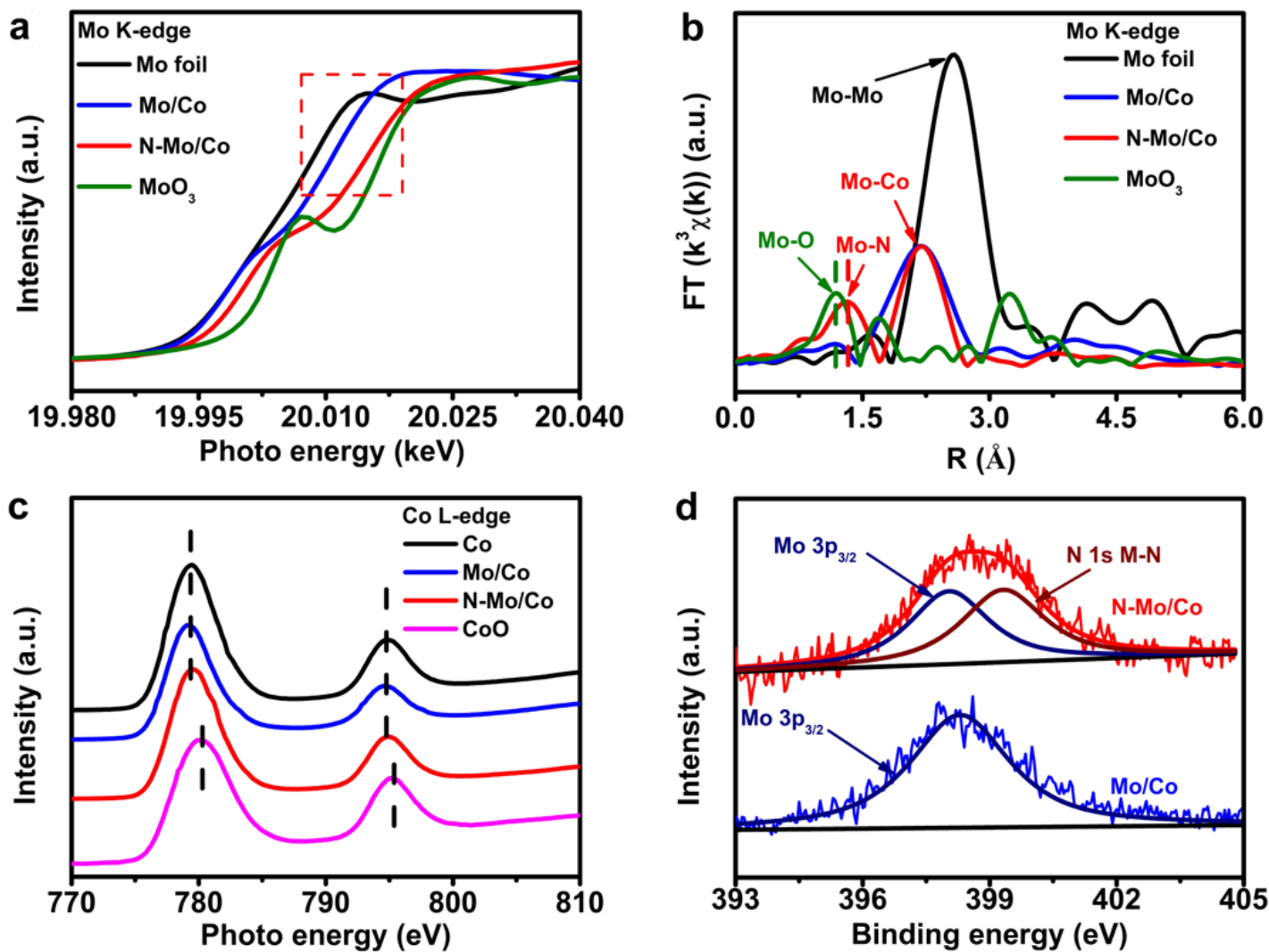


Figure 3

Chemical states and coordination structures of N-Mo/Co. (a) Mo K-edge. (b) Mo K-edge Fourier analysis. (c) Co L-edge of Co, Mo/Co and N-Mo/Co with CoO as reference. (d) N 1s and Mo 3p<sub>3/2</sub> XPS in N-Mo/Co.

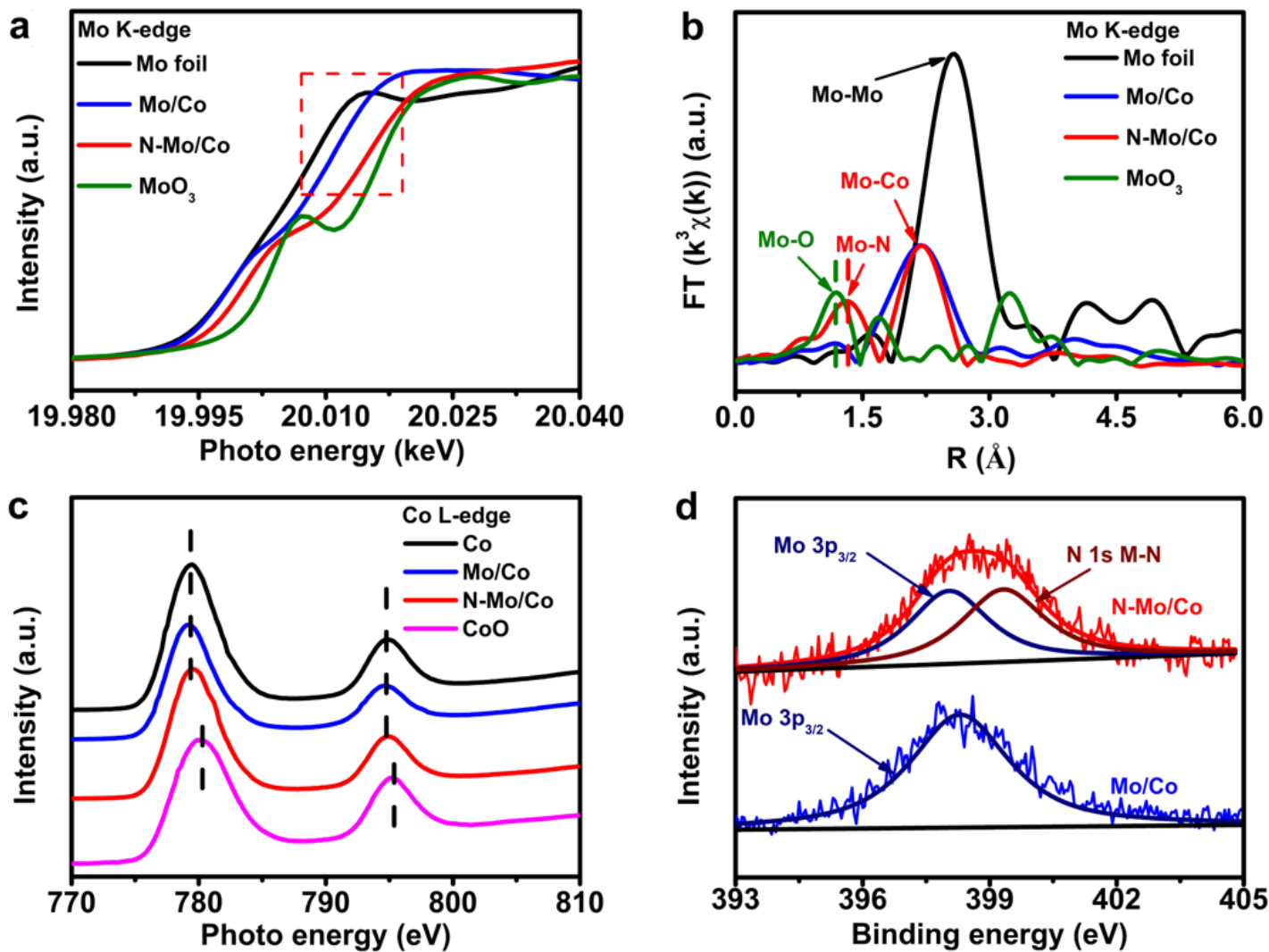


Figure 3

Chemical states and coordination structures of N-Mo/Co. (a) Mo K-edge. (b) Mo K-edge Fourier analysis. (c) Co L-edge of Co, Mo/Co and N-Mo/Co with CoO as reference. (d) N 1s and Mo 3p<sub>3/2</sub> XPS in N-Mo/Co.

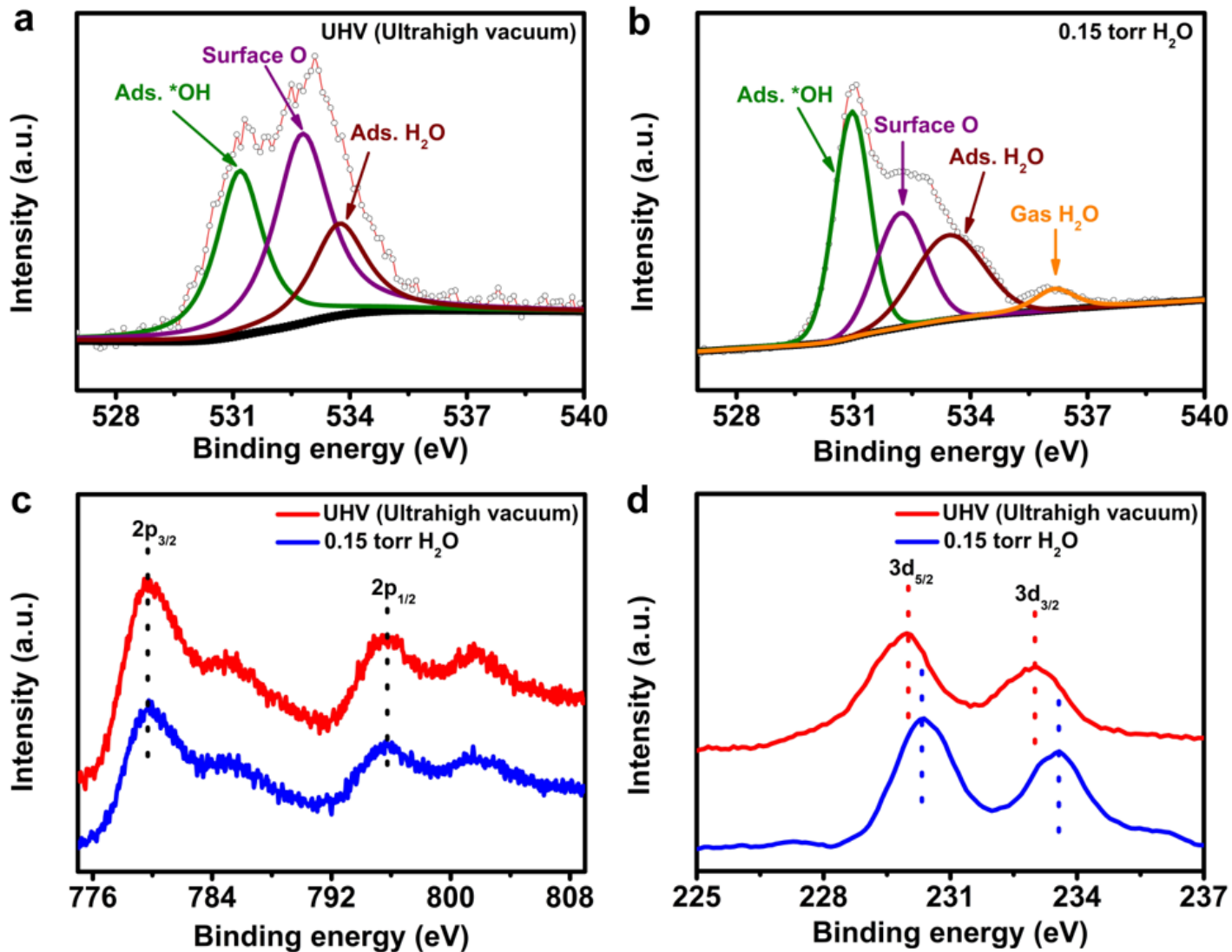


Figure 4

AP-XPS measurement of N-Mo/Co. (a) O 1s ambient pressure XPS of N-Mo/Co under UHV. (b) O 1s ambient pressure XPS of N-Mo/Co under 0.15 torr of water pressure. (c) Co 2p XPS spectra for N-Mo/Co under UHV and 0.15 torr of water pressure. (d) Mo 3d XPS spectra for N-Mo/Co under UHV and 0.15 torr of water pressure.

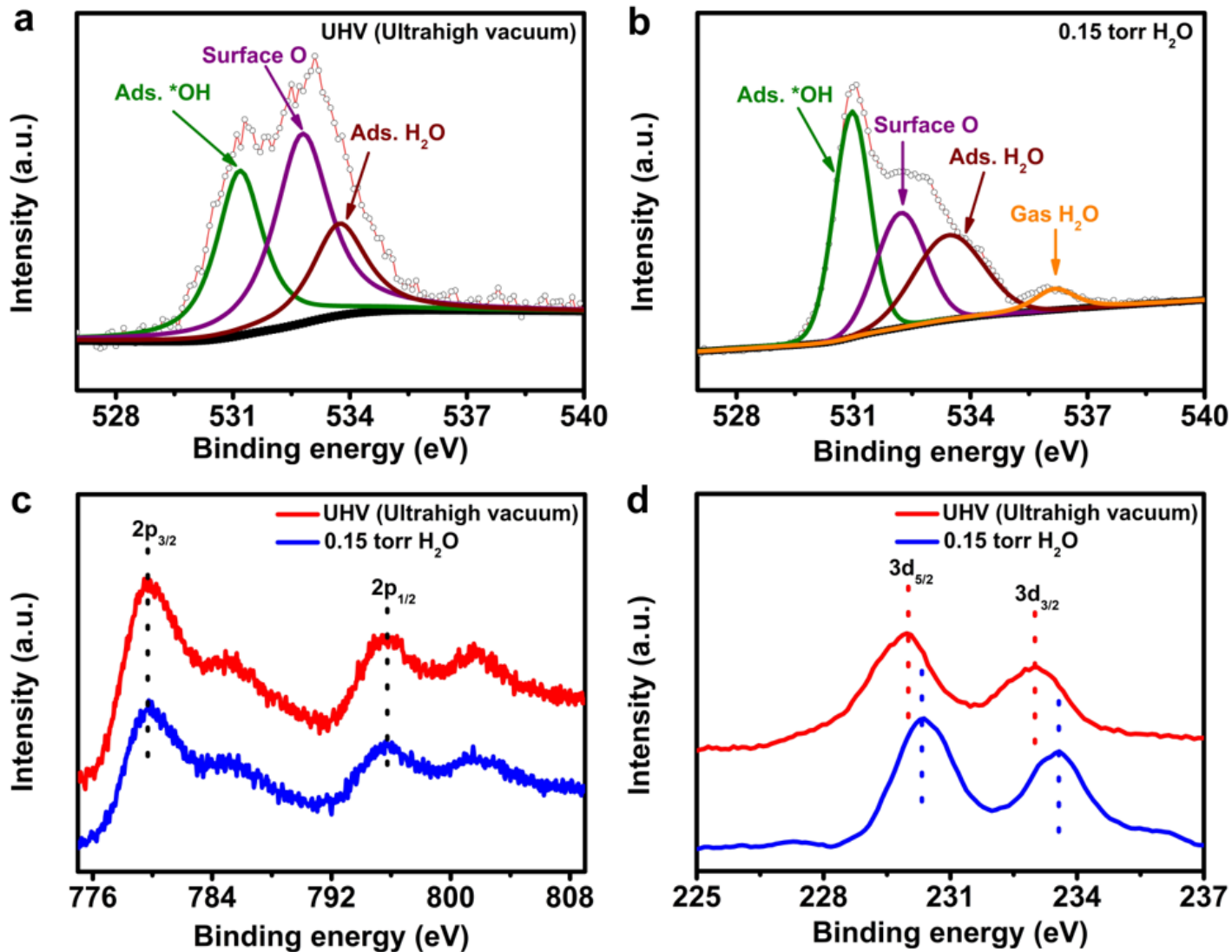


Figure 4

AP-XPS measurement of N-Mo/Co. (a) O 1s ambient pressure XPS of N-Mo/Co under UHV. (b) O 1s ambient pressure XPS of N-Mo/Co under 0.15 torr of water pressure. (c) Co 2p XPS spectra for N-Mo/Co under UHV and 0.15 torr of water pressure. (d) Mo 3d XPS spectra for N-Mo/Co under UHV and 0.15 torr of water pressure.

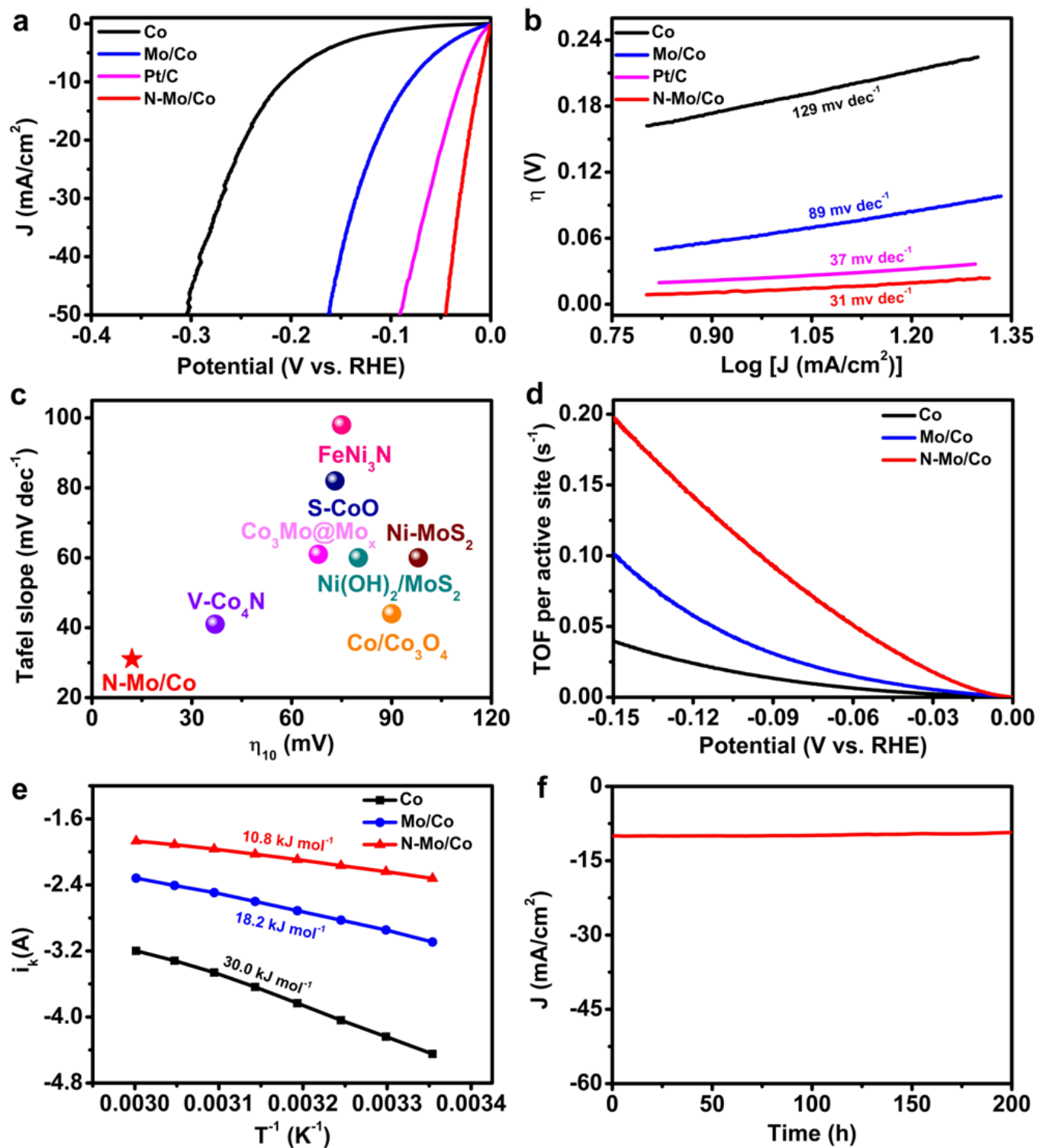


Figure 5

Alkaline HER performance of N-Mo/Co. (a) LSV of Co, Mo/Co, Pt/C and N-Mo/Co. (b) Tafel slopes of Co, Mo/Co, Pt/C and N-Mo/Co. (c) HER performance of N-Mo/Co with the ever-reported cobalt based materials. (d) TOF of Co, Mo/Co and N-Mo/Co. (e) Arrhenius plot of the kinetic current at  $\eta = 200$  mV of Co, Mo/Co and N-Mo/Co without  $iR$  correction. (f) Stability test of N-Mo/Co at the current density of 10 mA cm<sup>-2</sup>.

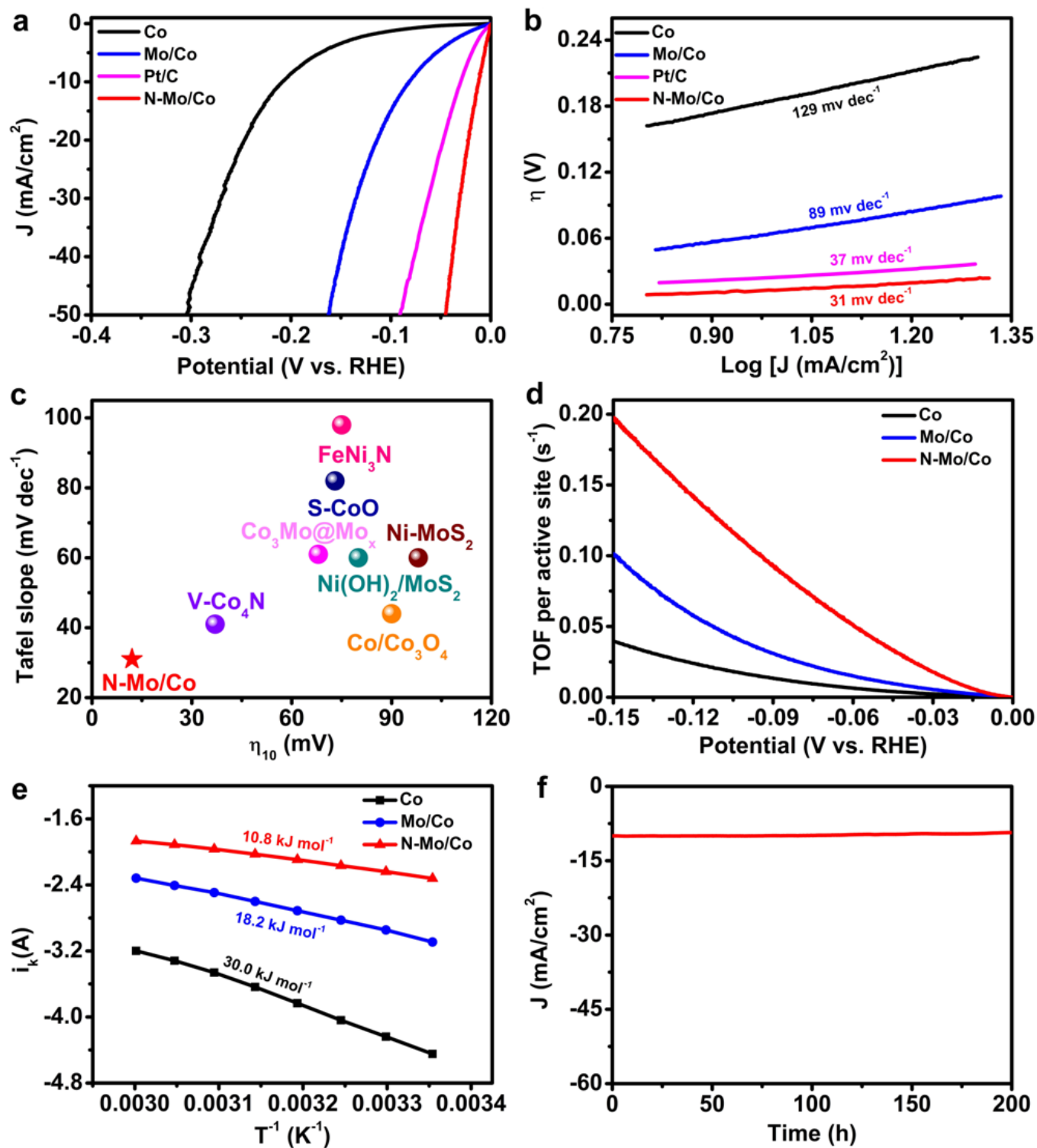


Figure 5

Alkaline HER performance of N-Mo/Co. (a) LSV of Co, Mo/Co, Pt/C and N-Mo/Co. (b) Tafel slopes of Co, Mo/Co, Pt/C and N-Mo/Co. (c) HER performance of N-Mo/Co with the ever-reported cobalt based materials. (d) TOF of Co, Mo/Co and N-Mo/Co. (e) Arrhenius plot of the kinetic current at  $\eta = 200$  mV of Co, Mo/Co and N-Mo/Co without  $iR$  correction. (f) Stability test of N-Mo/Co at the current density of 10 mA cm<sup>-2</sup>.

## Supplementary Files

This is a list of supplementary files associated with this preprint. Click to download.

- [SubmittoNatureCommunicationsSI.docx](#)
- [SubmittoNatureCommunicationsSI.docx](#)